IEEE Photonics Journal
An IEEE Photonics Society Publication

Open Access

Magnetic Field Measurement Using Peak-Locked Zeeman Coherent Population Trapping Resonance in Rubidium Vapor

Volume 11, Number 4, August 2019

Renu Tripathi
Gour S. Pati

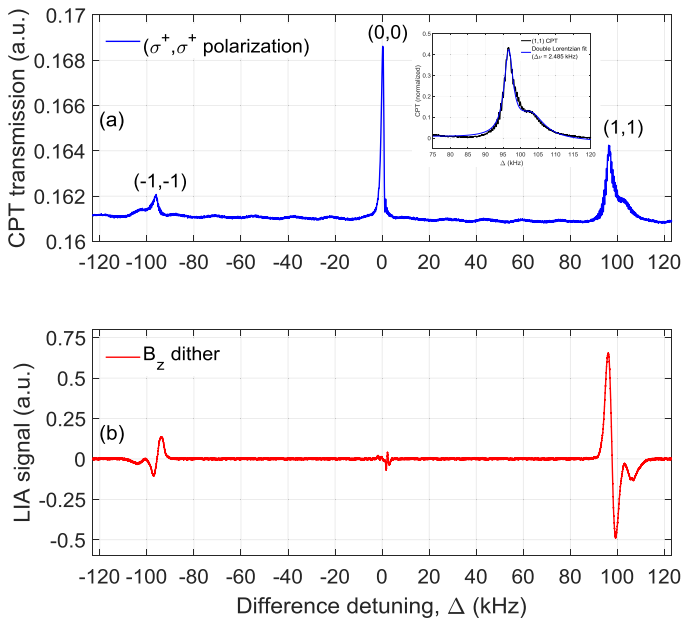

DOI: 10.1109/JPHOT.2019.2922831
1943-0655

IEEE photonics SOCIETY

IEEE

Magnetic Field Measurement Using Peak-Locked Zeeman Coherent Population Trapping Resonance in Rubidium Vapor

Renu Tripathi and Gour S. Pati

Division of Physical and Computational Sciences, Delaware State University, Dover, DE 19901 USA

DOI:10.1109/JPHOT.2019.2922831

Manuscript received May 3, 2019; revised May 28, 2019; accepted June 11, 2019. Date of publication June 13, 2019; date of current version July 2, 2019. This work was supported in part by NASA-EPSCoR under Grant 80NSSC17M0026, in part by NASA-MIRO under Grant NNX15AP84A, and in part by the DoD under Grant 62818-PH-REP. Corresponding author: Gour S. Pati (e-mail: gspati@desu.edu).

Abstract: A sensor for magnetic field measurement is developed using a small (centimeter size) rubidium cell. A high contrast Zeeman coherent population trapping (CPT) resonance is produced by the magnetic dither in the sensor solenoid, and a peak-locked servo is implemented for magnetic field measurement. Sensitivity close to 110 $\text{pT}/\sqrt{\text{Hz}}$ has been achieved in axial field measurement. The CPT-based magnetic sensor is capable of measuring sub-nanotesla level magnetic field variations at high (microtesla) field strength. We discussed possible sources of noise and broadening which are affecting the performance of the sensor, and suggest changes that will further improve the performance of the sensor.

Index Terms: Lasers and electrooptics, magnetooptic devices, photonics magnetics.

1. Introduction

Coherent population trapping (CPT) has been extensively studied in alkali atoms with a broad range of fundamental interests and applications relating to steep dispersion, ultralow group velocity, nonlinear optics at low light level, precision sensing, frequency referencing and others [1]–[6]. CPT is produced by Raman excitation with two coherent laser frequencies in a three-level $\Lambda-$system. Typically, a $\Lambda-$system is formed when two hyperfine ground states in the alkali atom are coupled to a common excited state by Raman excitation. For magnetic field sensing (or measurement), CPT formed between the ground state magnetic sublevels is used [7]–[13]. Similar to atomic frequency standards, magnetic field sensing using CPT provides high accuracy and sensitivity. Besides scalar magnetic field sensing, studies have shown that CPT-based approach can also be used to design vector magnetic field sensor [14], [15]. CPT also gives a practical advantage in designing an all-optical magnetic sensor (i.e., no RF excitation is needed [16]). Advances in miniaturized and micro fabricated alkali vapor cells are enabling significant reduction in the size of the CPT-based magnetic sensors and sensor arrays [10], [17]–[19].

High absolute accuracy in CPT-based magnetic sensor originates from the precise measurement of ground state hyperfine frequency in the alkali atom. The sensitivity of the magnetic sensor depends on the linewidth and the contrast of CPT resonance. The linewidth is fundamentally

determined by the inverse of the ground state coherence lifetime. In general, this is many milliseconds long in a buffer-gas filled vapor cell [8]. However, CPT linewidth observed in the experiment is typically larger than its fundamental linewidth, since it gets power broadened by higher optical power used to achieve higher contrast in the CPT resonance. Thus, there is a trade-off between CPT linewidth and its contrast. Furthermore, linewidth and contrast of Zeeman CPT resonance are affected by the magnetic environment of the cell. The linewidth is broadened by magnetic field inhomogeneity, and the contrast is affected by transverse field components. Despite these effects, CPT-based magnetic sensors have achieved high sensitivity ($\simeq 12$ pT/$\sqrt{\text{Hz}}$) using extremely narrow Zeeman CPT resonance (FWHM $\simeq$ 42 Hz) in a buffer-gas filled Cs cell [9]. More so, chip-scale CPT-based magnetic sensor (size $=$ 12 mm^3) with high sensitivity close 50 pT/$\sqrt{\text{Hz}}$ at 10 Hz has also been demonstrated [10]. Alternative optical excitation schemes, such as $lin \perp lin$, push-pull optical pumping and counter-propagating circularly polarized beams have been proposed for improving CPT contrast without broadening its linewidth [20]–[24]. However, these schemes are mostly applicable for magnetically-insensitive clock transition used in the CPT-based atomic frequency standards.

In this paper, we implemented a magnetic dither mechanism in servo control to demonstrate automated magnetic field sensing using peak-locked Zeeman CPT resonance. Magnetic dither generates dispersive Zeeman CPT signals with high contrast and signal-to-noise (SNR). The dispersive signal is then used as a feedback (or discriminant) to a phase-locked oscillator to perform magnetic field measurements. Compared to the common frequency dither approach, magnetic dither gives the advantage of discriminating magnetically-sensitive (Zeeman) CPT signal from magnetically-insensitive CPT signal, due to the fact that a small amplitude magnetic dither causes appreciable energy shift and strong modulation distinctly on the Zeeman CPT signal. Magnetic dither is also conducive for providing higher lock stability in CPT-based sensing since it does not require the oscillator to be perturbed during the locking. In our experimental demonstration, sensitivity close to 110 pT/$\sqrt{\text{Hz}}$ has been achieved in axial magnetic field sensing using a centimeter size rubidium cell of length 2.3 cm. The sensitivity of the sensor is currently limited by some of our design limitations, which are discussed later. We have also discussed how future design improvements will enable us to measure magnetic field variation at high fields with picotesla level (or higher) sensitivity. The paper is organized as follows. In Section 2, we provide a detailed description of our experimental design and performed measurements. In Section 3, we present results and discussions along with the performance and scope for future improvement of the sensor.

2. Experimental Description

Fig. 1 shows the diagram of the experimental setup used to produce CPT spectrum and measure axial magnetic field (B_z) using a peak-locked frequency servo. We used a pure-isotope ^{87}Rb vapor cell (optical length $=$ 2.3 cm, diameter $=$ 1 cm) filled with 10 Torr neon buffer gas. A tunable external-cavity diode laser (linewidth $<$ 1 MHz) was used as a light source. The laser is tuned to resonance with rubidium D1 transition ($\lambda \simeq 795$ nm). The laser beam is sent through a fiber pigtailed electro-optic modulator (EOM, bias $V_\pi = 1.4$ V) to produce a frequency-modulated laser beam with sidebands for conducting CPT experiment. The EOM is driven by a microwave oscillator consisting of a 10 MHz voltage controlled oscillator (VCO) and a phase-locked loop (PLL) for frequency up-conversion, to produce sidebands with frequency shifts close to half the ground-state hyperfine frequency (i.e., $\nu_{hf}/2 = 3.417$ GHz) of ^{87}Rb atoms. Therefore, the frequency difference ($\nu_{+1} - \nu_{-1}$) between the first-order optical sidebands matches the frequency $\nu_{hf} = 6.834$ GHz. CPT is produced by these two sidebands due to coherent $\Lambda-$transition in the rubidium cell (illustrated in Fig. 2). Multiple CPT resonances are observed by scanning the frequency difference between the two sidebands around ν_{hf} and measuring the transmitted light through the cell using a photodetector. Fig. 2 shows energy levels associated with the D1 manifold of ^{87}Rb atom and illustrates three CPT resonances which can be formed using optical excitations with circular polarizations of the form (σ^+, σ^+) for the two sidebands. These three resonances are labeled as $(-1, -1)$, $(0, 0)$ and $(1, 1)$ CPT resonances in terms of the quantum numbers of the corresponding ground-state sublevels.

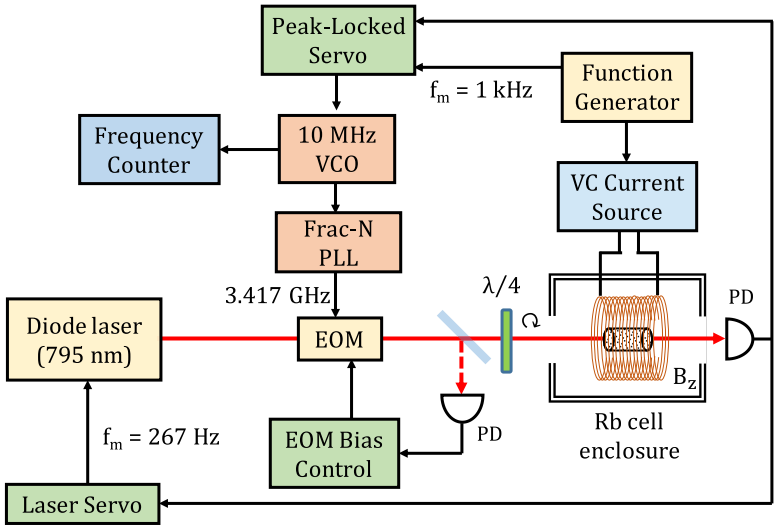

Fig. 1. Experimental setup for CPT-based magnetic field measurement. Axial magnetic field (B_z) is applied by placing the rubidium cell inside a solenoid.

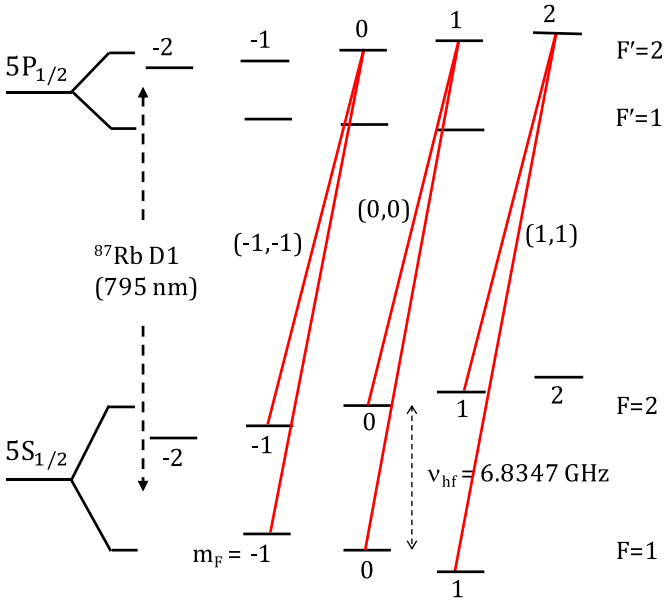

Fig. 2. Diagram showing multiple CPT resonances formed by $\Lambda-$transitions with (σ^+, σ^+) circular polarizations in the D1 manifold of ^{87}Rb atom.

In our experiment, we used the (1, 1) Zeeman CPT resonance for B_z measurement by virtue of its higher contrast with (σ^+, σ^+) excitation.

During the experiment, we locked the laser frequency to the maximum absorption (or minimum transmission) point of the Doppler-broadened ^{87}Rb D1 line produced by the modulated laser beam passing through the rubidium cell [25]. This gave us the convenience of using a single photodetector for implementing the laser servo as well as the peak-locked servo described later for magnetic field measurement. The laser servo is implemented via a direct dither of the piezo actuator in the laser cavity, and by designing a servo controller box consisting of a lock-in amplifier (LIA) and a proportional-integral (PI) controller. The presence of off-resonant carrier in the modulated laser

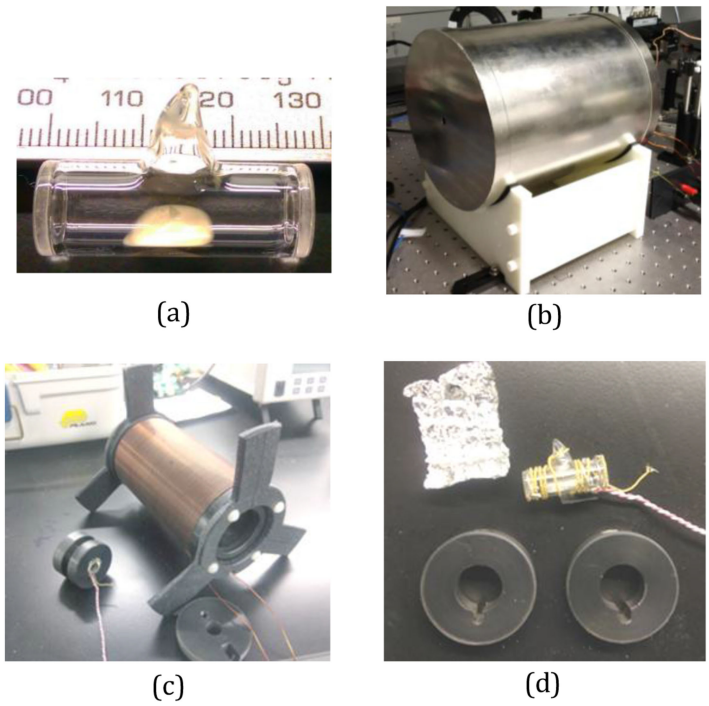

Fig. 3. Pictures showing different parts of the rubidium cell assembly and enclosure (a) rubidium cell, (b) three layer magnetic shield enclosure, (c) solenoid, and (d) cell heating arrangement and mounts.

beam produces a high background in the CPT signal. We minimized this background using an active feedback control on the EOM bias voltage [24]. This includes following steps: dithering the EOM bias voltage, picking off a small fraction of the beam after the EOM, measuring it with a photodetector, and sending the corrected voltage to the EOM produced by a servo similar to the laser servo. The servo allowed us to lock the EOM bias voltage to the minimum of the transmitted beam power, which satisfies the condition for minimum carrier as well. We neglected the effect of two-photon resonance of the second-order sidebands with the carrier due to the fact that power associated with the second-order sideband is substantially weaker than first-order. Suppressed carrier optical power produced by the EOM bias servo, was continuously monitored with a scanning Fabry-Perot etalon with FSR $=$ 10 GHz.

The rubidium cell assembly and enclosure were carefully designed to mitigate the effect of ambient noise on the magnetic field measurement. Fig. 3(a) shows a small rubidium cell which is enclosed in a custom-made three layer μ-metal magnetic shield enclosure. The enclosure (Fig. 3(b)) attenuates the ambient magnetic field resulting from the Earth and the local environment in the laboratory by more than 40 dB. The enclosure has an approximate cylindrical volume of 7000 cubic cm. We used a solenoid mounted inside the enclosure to apply a uniform axial magnetic field (B_z). Fig. 3(c) shows the solenoid with 60 turns of copper wire coiled around a plastic tube with spiraled grooves etched on its surface. The groove prevents the coiled wire from slipping and thus, helps in creating a uniform magnetic field along the axis of the solenoid. Three fins made on the ends of the solenoid allow it to be centered inside the μ-metal enclosure. The solenoid is driven by a low-noise voltage-controlled current source (CS580, SRS). We calibrated the current and the magnetic field produced by the solenoid using a sensitive fluxgate magnetometer (mag-03, Bartington instruments). The solenoid produced a uniform B_z with strength of roughly 40 mG for 7 mA applied current (slope $\simeq$ 5.71 A/G). Fig. 3(c) also shows the mounted rubidium cell placed on the left side of the solenoid. The cell is mounted inside two plastic discs using set-screws and then secured within the solenoid tube via pressure.

Prior to mounting the rubidium cell inside the discs, we wrapped the cell with bifilar twisted and polymide insulated nichrome heating wire (32 AWG, LakeShore cryotronics) as shown in Fig. 3(d). This reduces the residual magnetic field produced due to the cell heating coil. The cell was also wrapped in aluminum foil to retain the applied heat, and reduce the amount of current needed to maintain a steady cell temperature. Plastic end caps with holes for the laser beam and the wires, close off the solenoid tube to further reduce the temperature gradient and maintain a higher temperature stability across the cell. A programmable temperature controller (PTC10, SRS) was setup with the resistive nichrome heating wire and a standard K-type thermocouple sensor to actively control the cell temperature to within $\Delta T \simeq \pm 50$ mK. In order to find the optimal cell temperature, we measured the contrast of $(1, 1)$ CPT resonance as a function of varying cell temperature. We then maintained the cell at a steady and optimal temperature of 53 °C where the $(1, 1)$ CPT contrast was found to be maximum.

The laser beam used in the experiment was circularly polarized using a quarter ($\lambda/4$) waveplate. The beam emerging from the EOM was expanded and collimated using a beam expander to an approximate diameter of 8 mm before the cell. Expanded beam size and frequent collisions of ^{87}Rb atoms with Ne buffer gas atoms in the cell increased the interaction time of ^{87}Rb atoms with the laser beam, thus, preventing transit-time broadening of the CPT resonances [24]. We observed an approximate 3.022 kHz frequency shift in the peak of CPT resonance which is produced by the buffer gas. The difference frequency between the EOM sidebands is adjusted to account for this buffer gas induced frequency shift in the cell. Since our cell temperature is actively controlled to within an accuracy of 100 mK, the variation in this frequency shift due to temperature dependence of buffer gas is found to be negligible. Using the voltage-controlled current driver, we applied a bias current as well as a dither current ($f = 1$ KHz) to the solenoid. Bias current is independently adjusted to produce B_z with various strengths for our measurements. We measured B_z by locking the phased-locked microwave oscillator to the peak of $(1, 1)$ Zeeman CPT resonance. The phased-locked microwave oscillator consists of a stable 10 MHz VCO and a low phase-noise fractional-N phase-locked loop (Frac-N PLL, Texas Instruments). The PLL output is internally connected to an integrating servo (or loop filter) which locks the PLL's phase to the master 10 MHz VCO. Thus, under the peak-lock condition, a change in frequency of the 10 MHz VCO due to an applied B_z results in a proportional change in the PLL output frequency which allows us to measure B_z.

A sinusoidal voltage ($f = 1.860$ KHz) applied to the current source dithers the solenoid current to produce a dither in B_z, which in turn, produces a dither in the energy shift of the magnetic sublevels in ^{87}Rb atoms. As a result, the Zeeman CPT signals get amplitude modulated. We used a lock-in-amplifier (LIA) to demodulate the CPT signal at the dither frequency to observe high contrast dispersive (or derivative-like) CPT signal in the CPT spectrum. The full spectrum is observed by scanning the frequency of 10 MHz VCO using a voltage ramp. A PI controller was used to generate feedback signal required to lock the phase-locked oscillator driving the EOM to the peak of $(1, 1)$ Zeeman CPT resonance. A high resolution frequency counter is used to read the frequency shift of the locked oscillator away from 10 MHz. This frequency shift was simply multiplied by the PLL's frequency multiplication factor and converted to magnetic field B_z by dividing with a factor $2|g_F|\mu_B (= 1.399624$ MHz/G for $Rb) = 1.399624$ MHz/G, where g_F is the hyperfine g-factor (e.g., $-1/2$ for $\langle 5S_{1/2}, F = 1|$ and $+1/2$ for $\langle 5S_{1/2}, F = 2|$) and μ_B is the Bohr magneton frequency. We decided to choose different non-harmonic dither frequencies for the peak-locked servo ($f = 1.860$ KHz) and the laser servo ($f = 267$ Hz) in order to prevent lock instability caused by interference in the photodetector signals.

3. Results and Discussions

First, we calculated the CPT spectrum theoretically by solving the density matrix (or Bloch) equations for a multi-level ^{87}Rb atomic model [24], [26]. We included all sixteen energy levels associated with the D1 manifold in our model. We also included velocity averaging to account for atomic motion in the vapor medium. Fig. 4 shows the CPT spectrum generated by our model using resonant excitation of the $|F' = 2\rangle$ excited state with $|F = 1\rangle$ and $|F = 2\rangle$ ground states using (σ^+, σ^+) polarized light.

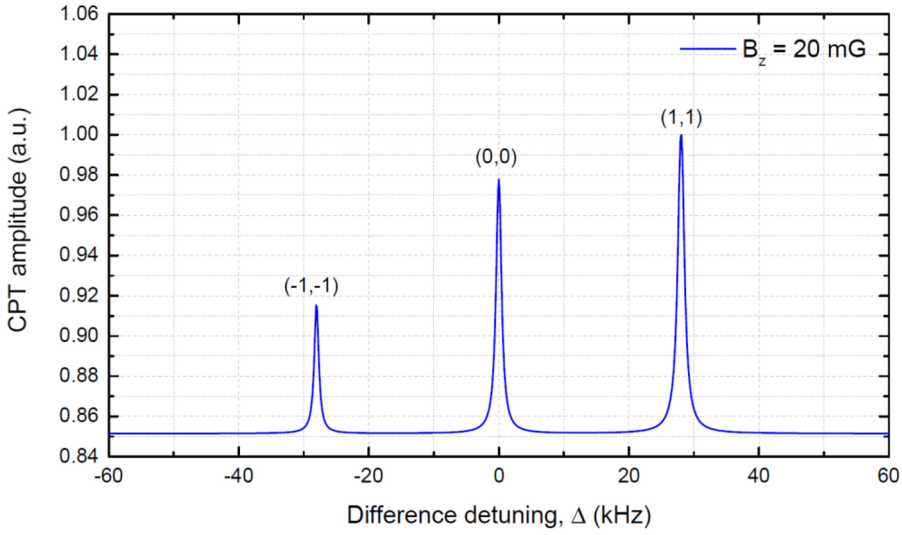

Fig. 4. Calculated CPT spectrum produced by resonant excitation of $|F' = 2\rangle$ excited state with $|F = 1\rangle$ and $|F = 2\rangle$ ground states using (σ^+, σ^+) polarized light for $B_z = 20$ mG.

We used following parameters in our calculations: excited state decay rate $\Gamma = 6$ MHz, equal Rabi frequencies $\Omega_+ = \Omega_- = \Gamma/60$ for the first-order sidebands in the modulated laser beam, empirical ground state decoherence rate $\gamma = 200$ Hz and a non-zero axial magnetic field $B_z = 20$ mG. The CPT spectrum is plotted as a function of the difference detuning Δ [$= (\nu_+ - \nu_-) - \nu_{hf}$]. The (0, 0) CPT peak is formed at $\Delta = 0$ and the (1, 1) and $(-1, -1)$ Zeeman CPT peaks are respectively formed at $\Delta = \pm 2\Delta_z$, where $\Delta_z = |g_F|\mu_B B_z$. The linewidths ($\Delta\nu$) of all three CPT resonances were obtained by using Lorentzian fittings to the plot. They were measured to be approximately 0.986 kHz for the (0, 0) CPT, 1.197 kHz for the (1, 1) CPT and 0.828 kHz for the $(-1, -1)$ CPT. These variations are due to the fact that CPT linewidth which is proportional to the square of average Rabi frequency, is defined by the normalized matrix elements associated with the Λ-transitions [26]. Additional narrowing of CPT linewidth occurs due to velocity averaging since most atoms are detuned away from the optical resonance. The calculated spectrum in Fig. 4 also reveals the relative contrast between the three CPT resonances. Maximum contrast is found in the $(+1, +1)$ CPT since it is closer to the $|F = 2, m_F = +2\rangle$ trap state having maximum population.

Fig. 5(a) shows experimentally observed CPT spectrum obtained by applying a bias current $I_b = 12$ mA ($B_z \simeq 69$ mG) to the solenoid. Fig. 5(a) shows strong amplitude modulated Zeeman CPT spectrum as a small dither is applied to the bias current I_b at 1.860 kHz. Fig. 5(a) shows all three CPT resonances, similar to the ones shown in Fig. 4. The $(-1, -1)$ and (1, 1) Zeeman CPT resonances are formed with central frequency shifts proportional to the applied B_z. As before, we measured the linewidth of (0, 0) CPT by doing a Lorentzian fit and found it to be approximately 1.483 kHz. The linewidth is broadened by the total optical power ($\simeq$100 μW) in the modulated laser beam. The linewidths of $(-1, -1)$ and (1, 1) Zeeman CPTs are broadened compared to the (0, 0) CPT due to magnetic field inhomogeneity over the cell length. There are two possible sources for magnetic field inhomogeneity (or gradient). In our system, it could be produced by the cell heater due to non-uniform wrapping of the heating coil around the small cell, and/or it could be created by 'image current' produced by the magnetic shield in the solenoid. The (1, 1) Zeeman CPTs is found to have a prominent narrow peak with a side hump. We measured the linewidth of (1, 1) CPT by doing a double Lorentzian fit (shown in Fig. 5(a)). The width of this prominent peak is found to be approximately 2.485 kHz, which is broadened nearly 1.7 times compared to the width of (0, 0) CPT. By measuring overall broadening of the (1, 1) CPT resonance, we estimated the magnetic field gradient along the cell to be approximately 0.3 μT/cm. We also measured the CPT contrast, C

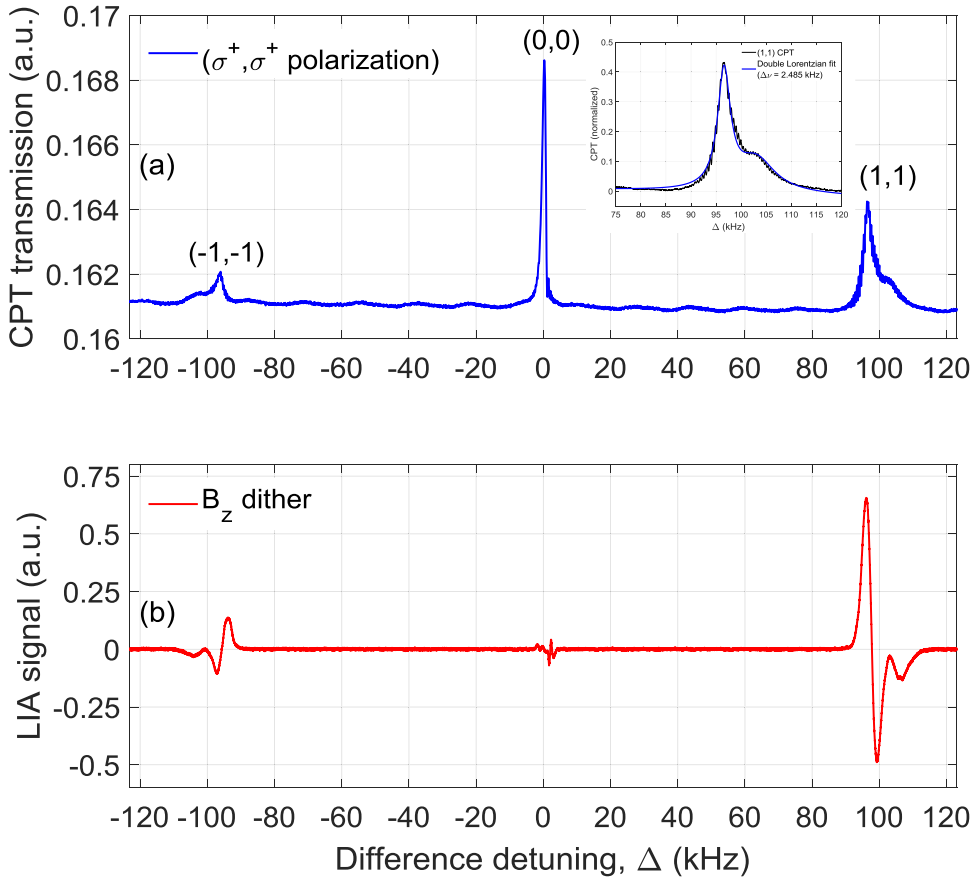

Fig. 5. (a) Amplitude modulated CPT spectrum produced by (σ^+, σ^+) excitation resonant with $|F' = 2\rangle$ excited state using $I_b = 12$ mA and a small dither in I_b at 1.86 kHz. The inset in the figure shows a Lorentzian fit of the central $(0, 0)$ CPT resonance, and (b) high-contrast dispersive Zeeman CPT spectrum obtained by using lock-in detection at 1.86 kHz.

by calculating $(V_P - V_B)/V_P$, where V_P and V_B are defined as the respective peak and background voltage levels of the CPT resonance. The contrast in $(0, 0)$ CPT is found to be $\simeq$4.5 %. The contrast in $(1, 1)$ Zeeman CPT is found to be $\simeq$2% and $(-1, -1)$ CPT is found to be $\simeq$0.6 %, which are smaller due to broadening caused by inhomogeneous magnetic field and also, due to the presence of transverse fields. This effect is not present in our simulation result since it did not consider the inhomogeneity (or gradient) and transverse fields. We used the $(1, 1)$ CPT signal in the experiment to perform B_z measurements.

Fig. 5(b) shows the CPT spectrum produced by performing demodulation of the photodetector output by a low-noise LIA at the dither frequency. The spectrum shows dispersive (or derivative-like) Zeeman CPT signals with high contrast and SNR [27]. The $(0, 0)$ CPT is not modulated since it is insensitive to magnetic field dither to the first-order. However, $(0, 0)$ CPT did produce a small dispersive signature in the spectrum due to its second-order magnetic field sensitivity. The spectrum also shows a flip in the slopes of $(-1, -1)$ and $(1, 1)$ dispersive signals simply due to opposite frequency shifts corresponding to change in I_b caused by the modulation. For performing B_z measurements, we sent the dispersive CPT signal from LIA to a PI controller. The output from the PI controller is used as a feedback signal to lock the frequency of 10 MHz VCO to the prominent peak of $(1, 1)$ CPT resonance. We measured the VCO frequency under the peak-locked condition with the frequency counter and calculated the frequency shift, $\Delta_z (= 2|g_F|\mu_B B_z)$ by subtracting the peak-locked VCO frequency from 10 MHz and multiplying the subtracted frequency with the PLL's

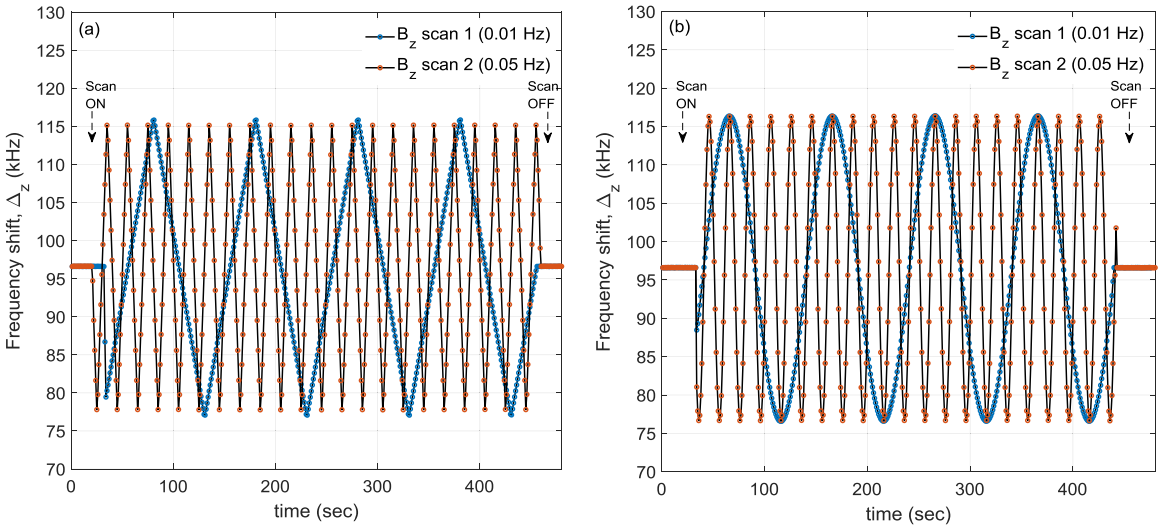

Fig. 6. Magnetic field scans performed using the peak-locked servo (a) linear B_z scan, and (b) sinusoidal B_z scan. The vertical axis in both plots correspond to the servo frequency shift Δ_z which is directly proportional to B_z.

frequency multiplier. The frequency shift, Δ_z is directly converted to the magnetic field intensity B_z by dividing it with $2|g_F|\mu_B$ ($=1.399624$ MHz/G)).

Fig. 6 shows frequency shift measurements performed using slow linear and nonlinear (sinusoidal) magnetic field scans. These scans were performed by sweeping the bias current, I_b to the solenoid with a function generator. Frequency measurements were performed at 1 Hz by setting the gate time to 1 sec on the frequency counter. Thus, the sensor is operated at 1 Hz bandwidth. It can be operated at higher bandwidth by appropriately setting the gate time on the counter. However, faster gate time reduces the precision in B_z measurement. Fig. 6(a) shows frequency measurement performed using two linear B_z scans at 0.01 Hz and 0.05 Hz, by using a voltage ramp. Different frequency shifts observed at the beginning of the scan are caused by different initial phases of the ramp generator at two frequencies. The frequency shift before the start of the scan corresponds to the magnetic field $B_z \simeq 69$ mG produced by the bias current $I_b = 12$ mA. After the scan is turned on, the frequency shift, Δ_z follows the linear scan of the bias current. The sensor automatically measures the variation in B_z due to its locked condition. Frequency fluctuations observed on the plot are possibly caused by current fluctuations in the cell heating coil, which is being actively controlled to maintain a steady cell temperature. Fig. 6(b) shows similar measurements performed using sinusoidal B_z scans at two different rates, 0.01 Hz and 0.05 Hz, respectively. These measurements could be interpreted as measurements of magnetic field variations associated with high field (in this case 69 mG) using the a peak-locked CPT-based magnetic sensor. Additional electronics can be used in the sensor to perform frequency sweep and automatic lock acquisition, thus, making it possible to automatically lock to higher field and measure magnetic field variations thereof, as required in various applications [28]–[30]. With a suitable phase-locked oscillator, the dynamic range of our CPT-based magnetic sensor can be made large ranging from sub-nanotesla to tens of microtesla, making it suitable for geomagnetic field surveying application.

Fig. 7 shows the sensitivity of the peak-locked CPT-based sensor in B_z measurement. This is obtained by calculating the power spectral density (PSD) of the PI controller voltage used in the servo control. The controller voltage is converted to units of magnetic field intensity in the PSD plot. The sensitivity in B_z measurement is estimated from the PSD plot to be approximately 110 pT/$\sqrt{\text{Hz}}$ at 1 Hz operating frequency of the sensor. Higher noise density is observed at frequencies below 10 Hz. Noise peaks at line frequency (60 Hz) and dither frequency (1860 Hz) are also visible in the PSD plot. To compare, we calculated the sensitivity of the sensor using the expression

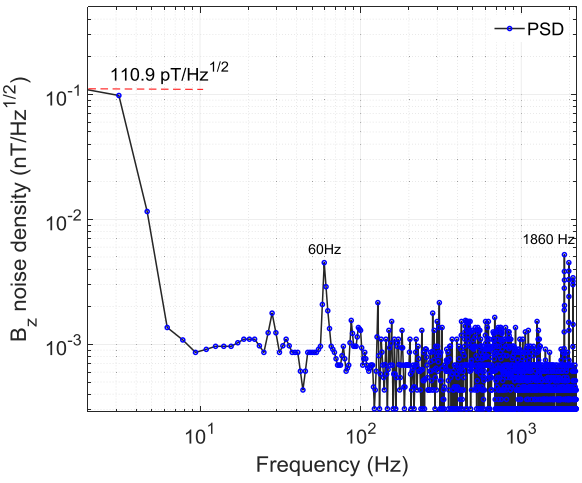

Fig. 7. Magnetic field sensitivity obtained by calculating the PSD of the PI controller voltage in the peak-locked servo.

$\Delta B_z = (1/2|g_F|\mu_B)(\Delta\nu/SNR)$, where $\Delta\nu$ and SNR are the respective linewidth and signal-to-noise ratio of the $(1, 1)$ dispersive CPT signal. To get the value of ΔB_z, we measured $\Delta\nu$ and SNR for the $(1, 1)$ dispersive CPT signal shown previously in Fig. 5(b). The linewidth was obtained from the peak-to-valley separation measurement to be approximately 2.5 kHz.

The SNR of the dispersive signal with one second averaging is found to be approximately equal to 400. With these numbers, the calculated value of ΔB_z is found to be 357 $\mathrm{pT}/\sqrt{\mathrm{Hz}}$, which is somewhat higher than the sensitivity estimated from the PSD plot. Several factors are currently influencing the sensitivity of the CPT-based magnetic sensor. Magnetic field inhomogeneity and transverse field distributions resulting from the cell heater and the field coil (solenoid) are broadening the Zeeman CPT resonance, thereby reducing the sensitivity. Measuring the magnetic field inside the solenoid using a fluxgate sensor showed an axial field gradient, potentially caused by the 'image current' due to the magnetic shield. Magnetic noise due to cell heater can be suppressed by using an ac cell heater operating at high frequency above the dither frequency. In this case, the magnetic noise due to ac heater will be averaged out over the measurement time. Additionally, a gradient coil can be used for cancelling (or nulling) any field gradient produced by the solenoid and/or the cell heater. Other sources of noise such as phase stability of the 10 MHz VCO, and magnetic field noise produced by current fluctuations in the cell heater can be mitigated using better instruments and careful designs. Cell with higher buffer gas pressure (up to 20–25 Torr) can be used to produce sub-kilohertz Zeeman CPT linewidth, which will further improve the sensitivity of the system. In future, we plan to incorporate all these changes, and also employ shot-noise limited signal detection technique to demonstrate picotesla (or higher) sensitivity using the CPT-based magnetometer.

4. Conclusion

We have demonstrated a CPT-based automated magnetic sensor for axial magnetic field measurement with sensitivity close to 110 $\mathrm{pT}/\sqrt{\mathrm{Hz}}$. Magnetic field measurements were performed using high-contrast dispersive Zeeman CPT signal produced by a peak-locked servo employing a magnetic dither mechanism. Measurement of magnetic field variation at high field has been demonstrated using a low-noise phase-locked oscillator. Performance of the CPT-based sensor showed that magnetic field variations can be measured with sub-nanotesla sensitivity. This can be further improved to meet applications that require monitoring magnetic field variations with high (picotesla) sensitivity at high (microtesla) field strength.

References

[1] E. Arimondo, "Coherent population trapping in laser spectroscopy," in *Progress in Optics*, vol. 35, E. Wolf, Ed. Amsterdam, The Netherlands: Elsevier, 1996, p. 257.
[2] R. W. Boyd, "Slow light and its applications," *J. Opt. Soc. Am. B.*, vol. 25, no. 12, pp. SL1–SL1, 2008.
[3] O. Schmidt, R. Wynands, Z. Hussein, and D. Meschede, "Steep dispersion and group velocity below c/3000 in coherent population trapping," *Phys. Rev. A, At. Mol. Opt. Phys.*, vol. 53, no. 1, pp. R27–R30, 1996.
[4] H. Schmidt and A. Imamoglu, "Giant Kerr nonlinearities obtained by electromagnetically induced transparency," *Opt. Lett.*, vol. 21, no. 23, pp. 1936–1938, 1996.
[5] J. Vanier, "Atomic clocks based on coherent population trapping: A review," *Appl. Phys. B*, vol. 442, pp. 421–442, 2005.
[6] M. S. Shahriar, G. S. Pati, R. Tripathi, V. Gopal, M. Messall, and K. Salit, "Ultrahigh enhancement in absolute and relative rotation sensing using fast and slow light," *Phys. Rev. A, At. Mol. Opt. Phys.*, vol. 75, no. 5, 2007, Art. no. 053807.
[7] M. Fleischhauer and M. O. Scully, "Quantum sensitivity limits of an optical magnetometer based on atomic phase coherence," *Phys. Rev. A*, vol. 49, no. 3, pp. 1973–1986, 1994.
[8] A. Nagel *et al.*, "Experimental realization of coherent dark-state magnetometers," *Europhys. Lett.*, vol. 44, no. 1, pp. 31–36, 1998.
[9] M. Stähler, S. Knappe, C. Affolderbach, W. Kemp, and R. Wynands, "Picotesla magnetometry with coherent dark states," *Europhys. Lett.*, vol. 54, no. 3, pp. 323–328, 2001.
[10] P. D. D. Schwindt *et al.*, "Chip-scale atomic magnetometer," *Appl. Phys. Lett.*, vol. 85, no. 26, pp. 6409–6411, 2004.
[11] C. Affolderbach, M. Stähler, S. Knappe, and R. Wynands, "An all-optical, high-sensitivity magnetic gradiometer," *Appl. Phys. B, Lasers Opt.*, vol. 75, no. 6/7, pp. 605–612, 2002.
[12] J. J. Song, S. Du, and B. A. Foreman, "Atomic magnetometer based on a double-dark-state system," *Phys. Lett., A, Gen., At. Solid State Phys.*, vol. 375, no. 37, pp. 3296–3299, 2011.
[13] Y. Hu, Y. Y. Feng, C. Xu, H. B. Xue, and L. Sun, "Loop-locked coherent population trapping magnetometer based on a fiber electro-optic modulator," *Appl. Opt.*, vol. 53, no. 10, pp. 2158–2162, 2014.
[14] K. Cox, V. I. Yudin, A. V. Taichenachev, I. Novikova, and E. E. Mikhailov, "Measurements of the magnetic field vector using multiple electromagnetically induced transparency resonances in Rb vapor," *Phys. Rev. A, At. Mol. Opt. Phys.*, vol. 83, no. 1, pp. 2–5, 2011.
[15] V. I. Yudin, A. V. Taichenachev, Y. O. Dudin, V. L. Velichansky, A. S. Zibrov, and S. A. Zibrov, "Vector magnetometry based on electromagnetically induced transparency in linearly polarized light," *Phys. Rev. A, At. Mol. Opt. Phys.*, vol. 82, no. 3, 2010, Art. no. 033807.
[16] E. B. Alexandrov, "Recent progress in optically pumped magnetometers," *Phys. Scr.*, vol. T105, no. 1, pp. 27–30, 2003.
[17] S. Knappe, "MEMS atomic clocks," in *Comprehensive Microsystems*, vol. 3, Y. Gianchandani, O. Tabata, and H. Zappe, Eds. Amsterdam, The Netherlands: Elsevier, 2007, pp. 571–612.
[18] J. Kitching, S. Knappe, and E. A. Donley, "Atomic sensors - A review," *IEEE Sens. J.*, vol. 11, no. 9, pp. 1749–1758, Sep. 2011.
[19] J. Kitching, "Chip-scale atomic devices," *Appl. Phys. Rev.*, vol. 5, May 2018, Art. no. 031302.
[20] Y. Y. Jau, E. Miron, A. B. Post, N. N. Kuzma, and W. Happer, "Push-pull optical pumping of pure superposition states," *Phys. Rev. Lett.*, vol. 93, no. 16, 2004, Art. no. 160802.
[21] S. V. Kargapoltsev, J. Kitching, L. Hollberg, A. V. Taichenachev, V. L. Velichansky, and V. I. Yudin, "High-contrast dark resonance in ??+-??- optical field," *Laser Phys. Lett.*, vol. 1, no. 10, pp. 495–499, 2004.
[22] K. Watabe, T. Ikegami, A. Takamizawa, S. Yanagimachi, S. Ohshima, and S. Knappe, "High-contrast dark resonances with linearly polarized light on the D_1 line of alkali atoms with large nuclear spin," *Appl. Opt.*, vol. 48, no. 6, pp. 1098–1103, 2009.
[23] Y. Yano and S. Goka, "High-contrast coherent population trapping based on crossed polarizers method," *IEEE Trans. Ultrason., Ferroelectr., Freq. Control*, vol. 61, no. 12, pp. 1953–1960, Dec. 2014.
[24] Z. Warren, M. S. Shahriar, R. Tripathi, and G. S. Pati, "Experimental and theoretical comparison of different optical excitation schemes for a compact coherent population trapping Rb vapor clock," *Metrologia*, vol. 54, no. 4, pp. 418–431, 2017.
[25] S. Goka, "85 Rb coherent-population-trapping atomic clock with low power consumption," *Jpn. J. Appl. Phys.*, vol. 48, no. 8R, 2009, Art. no. 082202.
[26] M. S. Shahriar, Y. Wang, S. Krishnamurthy, Y. Tu, G. S. Pati, and S. Tseng, "Evolution of an N-level system via automated vectorization of the Liouville equations and application to optically controlled polarization rotation," *J. Mod. Opt.*, vol. 61, no. 4, pp. 351–367, 2014.
[27] A.-L. Yang, G.-Q. Yang, Y.-F. Xu, and Q. Lin, "High contrast atomic magnetometer based on coherent population trapping," *Chin. Phys. B*, vol. 23, no. 2, 2014, Art. no. 027601.
[28] J. Belfi, G. Bevilacqua, V. Biancalana, Y. Dancheva, and L. Moi, "All optical sensor for automated magnetometry based on coherent population trapping," *J. Opt. Soc. Amer. B*, vol. 24, no. 7, pp. 1482–1489, 2007.
[29] V. Acosta *et al.*, "Nonlinear magneto-optical rotation with frequency-modulated light in the geophysical field range," *Phys. Rev. A, At. Mol. Opt. Phys.*, vol. 73, no. 5, 2006, Art. no. 053404.
[30] L. Lenci, S. Barreiro, P. Valente, H. Failache, and A. Lezama, "A magnetometer suitable for measurement of the Earth's field based on transient atomic response," *J. Phys. B, At. Mol. Opt. Phys.*, vol. 45, no. 21, 2012, Art. no. 215401.